Environmental Science & Technology

Article

pubs.acs.org/est

Selenium Speciation in Framboidal and Euhedral Pyrites in Shales

Adriana Matamoros-Veloza,* Caroline L. Peacock, and Liane G. Benning*

Cohen Geochemistry Laboratory, School of Earth and Environment, University of Leeds, Leeds LS2 9JT, U.K.

Supporting Information

ABSTRACT: The release of Se from shales is poorly understood because its occurrence, distribution, and speciation in the various components of shale are unknown. To address this gap we combined bulk characterization, sequential extractions, and spatially resolved μ-focus spectroscopic analyses and investigated the occurrence and distribution of Se and other associated elements (Fe, As, Cr, Ni, and Zn) and determined the Se speciation at the μ-scale in typical, low bulk Se containing shales. Our results revealed Se primarily correlated with the pyrite fraction with exact Se speciation highly dependent on pyrite morphology. In euhedral pyrites, we found Se(-II) substitutes for S in the mineral structure. However, we also demonstrate that Se is associated with framboidal pyrite grains as a discrete, independent $FeSe_x$ phase. The presence of this $FeSe_x$ species has major implications for Se release, because $FeSe_x$ species oxidize much faster than Se substituted in the euhedral pyrite lattice. Thus, such an $FeSe_x$ species will enhance and control the dynamics of Se weathering and release into the aqueous environment.

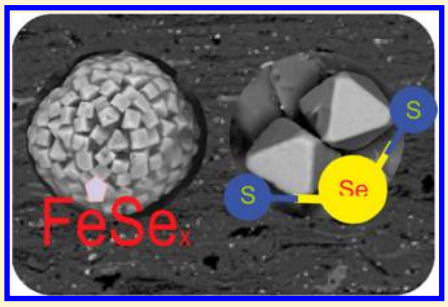

INTRODUCTION

Selenium (Se) is an essential micronutrient but only within a very narrow concentration range, above which it is toxic.[1] Selenium is an antioxidant that prevents tissue damage and aids growth and metabolic processes;[2] however, an intake dose above 450 μg/day Se can disrupt dermal and neurological processes and ultimately be fatal.[3,4] The use of Se contaminated groundwaters for drinking and Se contaminated soils for agricultural purposes introduces Se into the human food chain. Se poisoning has been reported at several locations with extreme cases in China (Yutangba),[5] India (Punjab), and in Colombia (Villeta).[6−8] In order to help prevent future health hazards related to Se toxicity, we need to improve our understanding of the factors and mechanisms that control its fate and mobility in the environment.

A variety of geological and geochemical factors have been suggested as possible controls for the release of Se from rocks (e.g., rock type, weathering environment, groundwater composition, organic matter content, Fe or Se speciation, etc.).[5,9,10] In Se-enriched surface environments, shales are an important source of Se to soils.[5,8,11,12] However, the transfer of Se from shale rocks into soils and groundwaters[5] and ultimately to humans via the food chain[6] is poorly constrained. Furthermore, the role of geological settings or specific geochemical reactions leading to the sequestration of Se in shale components are also poorly understood. This is because Se chemistry is highly complex. Selenium occurs in four principal oxidation states -II, 0, IV, VI, but Se(-I) compounds have also been found in nature and Se(II) compounds can be produced synthetically. Se has also six stable isotopes and is therefore of interest as a palaeoenvironmental proxy.[12] The most oxidized species, Se(IV) and Se(VI), occur as the oxyanions selenite ($SeO_3^{=}$) and selenate ($SeO_4^{=}$), and they are the most soluble, reactive, bioavailable, and therefore the most toxic Se species. Depending on their molecular bonding environment, different Se species have been suggested to be associated (either surface adsorbed or structurally incorporated) with various possible Se hosting phases.[13−15] In shales, the three main host components of Se are inferred to be silicates, organic matter (OM), or sulfides (primarily pyrite). Organic matter (kerogen fraction) has been suggested as a Se host in shales that are exceptionally Se and carbon rich and linked to coal beds.[15] However, neither the importance of OM as a Se host, nor a clear correlation between Se and OM in typical black shales, with average lower Se concentrations, have so far been demonstrated. Conversely, several studies proposed pyrite as the possible Se host mineral in shales,[5,8,16,17] yet a mechanistic or speciation related explanation is still lacking. Experimental studies[18−21] suggested that Se is likely either adsorbed/reduced on preformed pyrite grains or structurally incorporated into the sulfide phase.[22,23] However, a detailed mechanistic reaction pathway that addresses the uptake of Se into pyrite during pyrite growth, and a Se speciation and detailed structural and molecular bonding environment regardless of pyrite formation pathways, is still lacking. This is despite the fact that pyrite is a well-known sink for metals, and, specifically, the accumulation of Se in shales may be used as a tool to interpret palaeo-ocean chemical signals.[12,21]

To better understand Se sequestration and speciation in shales, we examined the distribution of Se and other elements (Fe, As, Cr, Ni, and Zn) in typical shales using bulk geochemical and sequential extractions techniques and combined these with a detailed quantification of the Se speciation in shale-associated pyrite grains at the μ-scale using synchrotron-based μ-X-ray fluorescence (μ-XRF) and μ-X-ray absorption spectroscopy (μ-

Received: December 30, 2013
Revised: July 16, 2014
Accepted: July 17, 2014
Published: July 17, 2014

 © 2014 American Chemical Society

Table 1. Concentration of Se (μg/g) in the Principal Fractions in the Shale Samples As Derived through Application of Protocols A and B and the $Cr(II)Cl_2$ Extraction

	Protocol A - Se(μg/g), (%)[a]				Protocol B - Se(μg/g), (%)[a]	Se(μg/g)
		Base soluble	Residual		Sulfides + Organics	
	Bulk Se μg/g	Tightly bound Se(IV), organic and inorganic selenides	Sulfides, recalcitrant organic matter, silicates	% OM+Sulfides[b]	Sulfides and Organics	Se in Sulfides $Cr(II)Cl_2$
UK1	3.13	2.48 (79)	0.29 (9.9)	88	3.70 (118)	1.57 (50)
UK2	9.77	6.51 (67)	2.80 (29)	96	9.43 (97)	7.22 (74)
UK3	1.29	0.71 (55)	0.25 (19)	74	1.00 (77)	0.59 (46)
UK4	0.83	0.27 (33)	0.49 (59)	92	0.78 (94)	0.17 (20)
UK5	3.87	3.47 (90)	0.17 (4.4)	94	3.63 (94)	

[a]In parentheses shown are the % Se in each fraction as a fraction of the total bulk Se. Percentage of Se in the extraction in relation to the bulk Se, % = (fraction *100)/bulk Se. [b]Sum of % Se base soluble + residual.

XAS). Our objectives were (1) to quantify the speciation and chemical environment of Se in shales, (2) to demonstrate a link between Se occurrence, distribution and sulfide morphology, and (3) to derive likely chemical pathways for both the accumulation and release of Se in/from shales.

■ EXPERIMENTAL SECTION

Samples, Bulk Characterization, and Se Analyses. We characterized five shale samples from West Yorkshire, UK[24,25] (samples identified as UK-1 to UK-5; Table S1). Powdered and homogenized samples were analyzed for their mineralogical composition (by X-ray diffraction, XRD), major elemental composition (by bulk X-ray fluorescence, XRF), and trace element concentrations (by digestion and inductively coupled plasma mass spectrometry, ICP-MS). Furthermore, we used elemental analyses to determine total and organic carbon, total and reduced inorganic sulfur, and full digestion and hydride generation atomic absorption spectroscopy (HG-AAS) to determine the bulk Se content in each sample. The morphologies of sulfide grains in each sample were identified using electron microscopy and Se concentrations in ∼20−40 individual pyrite grains, and a few control points (2−3) on the silicate and organic matter were analyzed by electron microprobe (EMPA). Full details on the geological settings, the formation conditions (i.e., redox etc.), and all methods employed are given in the Supporting Information (SI).

Sequential Extractions and Total Digestions. To quantify the Se concentrations associated with different shale fractions, we applied various extraction protocols using progressively stronger reagents that extract Se associated with specific mineral and/or organic fractions.[16] Protocol A consisted of a modified six-fraction scheme:[17] water-soluble (H_2O − Se(IV), Se(VI), organic-Se), ligand exchangeable (K_2HPO_4/KH_2PO_4 − Se(IV) in oxides and clays), base soluble (NaOH − tightly bound Se(IV) and selenides), elemental selenium (Na_2SO_3 − Se(0)), acetic acid soluble (CH_3COOH − Se in calcite and gypsum), and residual ($HF/H_2O_2/HNO_3$ − Se in sulfides, recalcitrant organic matter, and in silicates). Protocol B followed a four-fraction scheme:[26] water-soluble/exchangeable (H_2O − Se(IV), Se(VI), organic-Se), oxides ($NH_2OH{\cdot}HCl$ − hydrous Fe−Mn oxides), sulfides/organics ($KClO_3$), and residual ($HF/H_2O_2/HNO_3$ − silicates, carbonates, and gypsum). We also carried out a one-step extraction/reduction with $Cr(II)Cl_2$[27] to quantify Se in diselenides and sulfides. The solutions resulting from each extraction step were analyzed for their Se contents using HG-AAS.[16]

Se Speciation. Based on the results from the bulk and sequential analyses described above, we selected the two samples with the highest bulk Se contents (UK-1 and UK-2) for the Se speciation analyses using synchrotron-based μ-XRF and μ-XAS. Polished sections of both samples and 11 standards (prepared as pressed pellets with 6% Se in boron nitride; CAS numbers and chemical formulas in Table S2 in the SI) representing four Se oxidation states and Se-organic species were analyzed on beamline I18 at the Diamond Light Source Ltd., UK (full details of beamline set up in the SI).

Using μ-XRF we endeavored to map in each sample ∼3−5 areas of interest (100 × 100 μm, 150 × 150 μm or 350 × 450 μm). These areas contained various preidentified pyrite morphology assemblages, and in each map the distribution of Se, Fe, Ni, Cu, Zn, and As was measured. The μ-XRF beam spot size was 5 × 6 μm, and the maps were collected using a step size of 5 μm, and an integration time of 1000 ms. Despite multiple attempts we were only able to collect statistically relevant data for sample UK-2, because the fluorescence signal to quantify Se in sample UK-1 was too low. In the various areas of interest in sample UK-2 we identified multiple points of interest (POI) representing either euhedral or framboidal pyrite grains. At each of these POI 12 μ-X-ray absorption near edge spectra (μ-XANES) collected at the same x and y coordinates confirmed there was no beam-induced sample damage or changes in Se oxidation state as a result of μ-XANES measurement (Figure S1). We then selected 14 specific POI that showed strong correlations between Se and the other measured elements and recorded at each of these POI four μ-XANES scans with a step size of 0.4 eV and beam spot size of 5 × 6 μm. From these 14 POI (Table S3 in the SI) only four gave a Se absorption edge jump above 0.1, and we selected two POI for further μ-EXAFS analyses. POI*a* was a typical euhedral pyrite grain and POI*b* represented framboidal pyrite grains. At both POI we collected 16 μ-EXAFS scans at the Se K-edge.

The μ-XANES spectra were averaged, normalized, calibrated, and compared with standards using the inflection point of the first derivative, the position of the white line and the second peak of the fingerprint as a reference. The energy of the monochromator was calibrated with an Au foil, and the K-edge energy for trigonal Se(0) was determined to be 12650 eV. Before processing and analysis, our XANES and EXAFS data were calibrated to the theoretical value for Se(0) of 12658 eV. The μ-

Table 2. EMPA Analysis of Se (ppm) in Individual Pyrite Grains (with Morphological Splits) Compared to Bulk Se Concentrations (UK-5 Contained No Pyrite; See Also SI Tables S3 and S4)[a]

		Se, ppm individual grains (undifferentiated)				Se, ppm individual grains, framboidal aggregates				Se, ppm individual grains, euhedral			
sample	Se bulk ppm	mean	min.	max.	no. of analyzed points[b]	mean	min.	max.	no. of analyzed points[b]	mean	min.	max.	no. of analyzed points[b]
UK-1	3.13	255	100	561	29 (<DL = 5)	192	110	300	15 (<DL = 5)	661	100	561	14
UK-2	9.77	365	110	670	42 (<DL = 8)	309	110	510	27 (<DL = 6)	413	190	670	15 (<DL = 2)
UK-3	1.29	171	110	310	20 (<DL = 12)	171	110	310	20 (<DL = 12)				0
UK-4	0.83	164	120	200	26 (<DL = 17)				12 (<DL = 12)	164	120	200	11 (<DL = 2)

[a]Left, middle, and right panels include basic statistics for Se concentrations with no differentiation in morphology vs framboidal and euhedral pyrites, respectively. [b]DL = limit of detection, 90 ppm; points below DL were excluded from the statistical analyses.

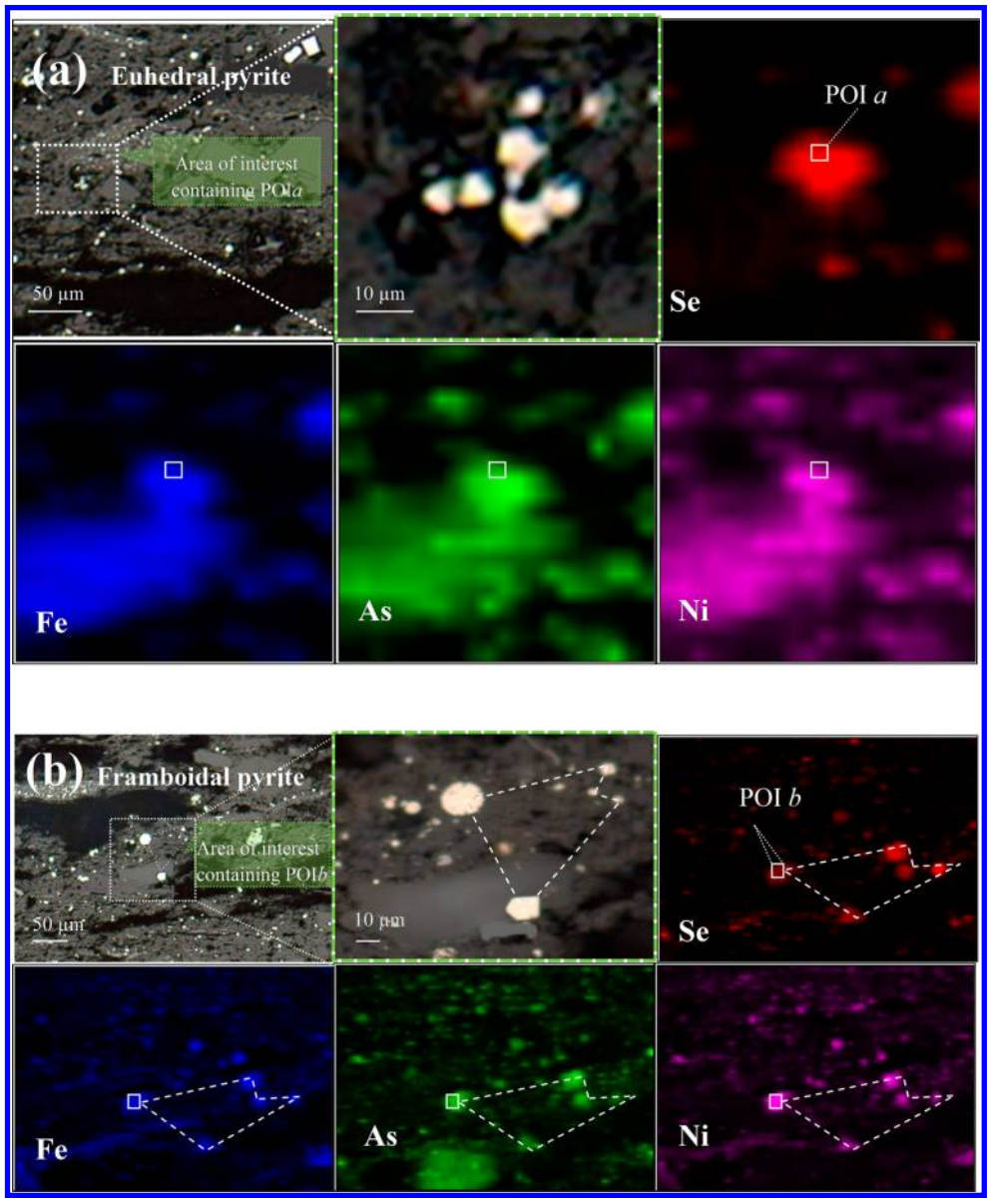

Figure 1. Light microphotographs of the μ-XRF areas of interest and corresponding μ-XRF elemental maps around POI*a* (top) and POI*b* (bottom). The enlarged areas next to them were imaged using the microscope on the beamline set at 45 deg, hence the slight offset. Similarly, the distortion between these enlarged area images and the X-ray maps is due to the fact that the beamline camera and the incident X-ray beam see the sample at different incident angles. In the enlarged image and the X-ray maps for POI*b* the dotted lines are just to guide the eye and show the distortion.

EXAFS spectra were averaged, background subtracted, and fitted to various theoretical models. Initial fits using Se−C or Se−Se[28] bond distances were unsuccessful, and thus organic and elemental Se were discarded from the subsequent fits. The remaining possibilities were either Se(-I) or Se(-II) most likely in sulfides, and we included several atoms (Fe, S, and Se) and

variable numbers of shells at close proximity to Se, similar to the approach of Ryser et al.[29] Specifically, we trial fitted our spectra using the models of pyrite[30] and marcasite[30] (FeS_2) and also ferroselite[31] ($FeSe_2$) but fits to marcasite were not successful. We did not fit our spectra to dzharkenite (a ferroselite polymorph FeS_2),[29] because this model has Se−Se distances of 2.28 Å and our very first tests showed no fit to Se−Se distances for the first shell. Further details of the μ-XANES and μ-EXAFS data analysis are presented in sections 9 and 10 in the SI.

RESULTS

Bulk Composition and Se Distribution in the Various Shale Fractions. The elemental and mineralogical analyses of all samples (Tables S4−S6 and Figure S2 in the SI) revealed the presence of high proportions of silicates (∼44−96%), medium to low contents of sulfides (∼1−5% pyrite, confirmed by the ∼1−3% reduced inorganic S contents), and low total organic carbon contents (TOC = 2−5%). Sample UK-5 was lacking pyrite (or reduced S), and, besides silicates, the second dominant phase was calcite. The bulk Se concentrations varied between ∼0.8 and ∼10 μg/g with the highest values found in samples UK-1 (3.13 ppm), UK-2 (9.77 ppm), and UK-5 (3.84 ppm). All samples were enriched in trace elements (Table S7 in the SI), and Se significantly correlated with Ni (correlation coefficient: 0.79), Cu (0.76), Cr (0.83), and V (0.81).

Se Distribution. The sequential extraction results (Table 1, Figures S3 and S4 in the SI) are particularly interesting for the samples with highest bulk Se concentrations. The base soluble and residual fractions (protocol A) and the sulfide and organic fractions (protocol B) showed between ∼74−118% of the total bulk Se associated with sulfides or organic matter (Table 1, Figure S4 in the SI). Sample UK-5 contained no inorganic sulfur or pyrite and was not further pursued. In UK-1 and UK-2, the next extraction revealed that 50 and 74% respectively of the total Se was sulfide associated, yet the remaining Se was not solely associated with organic matter (Table 1 and Figure S4 in the SI).

Se in Individual Pyrite Grains and the Matrix. Samples UK-1 to UK-4 all contained pyrite as both euhedral and framboidal morphologies. The Se concentration in individual framboidal or euhedral grains was typically ∼1−3 orders of magnitude higher than the bulk concentration (Table 2 and Table S8 in the SI). Selenium in "non-pyrite" control points (i.e., silicates and organic matter; total of 12 analyses in the 4 pyrite containing samples) was below detection, corroborating that pyrite was the prime carrier of Se and cross-confirming the sequential extraction data (Table 1). Not surprisingly, sample UK-2 (highest bulk Se content) showed the highest mean Se concentration in individual grains (670 ppm). Although Se concentrations varied greatly between the two morphologies or within the same morphological type in a single sample, overall Se concentrations tended to be higher in euhedral grains (Table 2 and Table S8 in the SI). Because of the close link between shale pyrite weathering and Se release,[8,12,22,23,29] hereafter we focused our Se μ-XAS analyses solely on samples UK-1 and UK-2. These represent typical shales containing pyrite and organic matter (Table S6 in the SI) and the highest bulk Se concentrations among the samples studied.

Elemental Distributions and Correlations at the μ-Level. From the five μ-XRF elemental maps in sample UK-2, two areas of interest (Figure S5 in the SI) were selected for higher resolution μ-XRF mapping (Figure 1) and revealed statistically significant correlations between Se, Fe, As, Ni, and Cu (Figure S6 and Table S9 in the SI) in the pixels on or in close vicinity to pyrite grains.

Se Oxidation States. The μ-XANES spectra of the 14 POI in the highest resolution μ-XRF maps in sample UK-2 revealed spectral fingerprints (inflection point of the first derivative, position of the white line peak at the absorption edge) qualitatively similar to the seleno-L-cysteine, Se sulfide, elemental Se, and synthetic ferroselite[29] standards (Figures S7 and S8). Two particular areas with framboidal (POI*a*) and euhedral grains (POI*b*) were selected for further μ-XANES analyses (Figure 2).

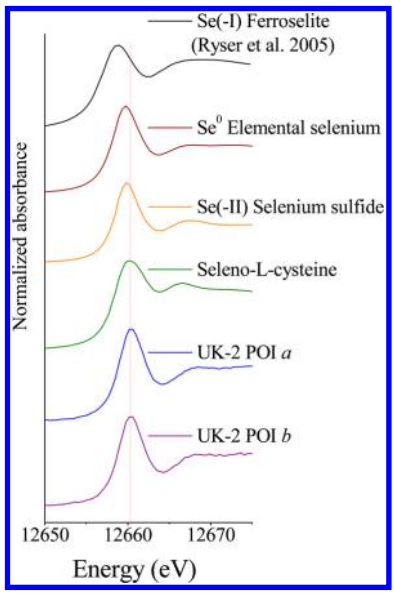

Figure 2. Se K-edge μ-XANES spectra from POI*a* and POI*b* and selected standards. We also included the Se(-I) ferroselite standard from Ryser et al.[29] but note that the spectral position in this spectrum is offset, yet the general shape and amplitude of the spectrum can be compared with our data.

The X-ray energy at the inflection point in both POI*a* and POI*b* (12658.5 eV) was very close to that in the Se(-II, 0) standards (12658.0 eV). The X-ray energies at the peak of the white line (12660.6 eV for POI*a* and 12660.2 eV for POI*b*) were also very similar to the standards (12660.2 eV for seleno-L-cysteine; 12660.2 eV for elemental Se(0); 12659.7 eV for Se(-II) sulfide). On visual inspection, the spectral fingerprints of POI*a* and POI*b* were very similar to the Se(-II) sulfide standard and also showed close similarity to the elemental Se(0) standard. POI*a* and POI*b* were, however, less similar to seleno-L-cysteine. Comparing with the synthetic ferroselite spectra,[29] the overall fingerprint was similar. We did not align the Ryser et al.[29] spectrum with our spectra as the details of beamline set up were unavailable, although, to the best of our knowledge, the ferroselite spectrum was collected with a step size of 0.7 eV.[29] Despite the similarities between POI*a* and POI*b* and Se(-II) sulfide, Se(-I) ferroselite, and elemental Se(0), it was not possible to determine the oxidation state, or the local coordination environment, of Se in our samples as the uncertainty of the data at the XANES region was 0.4 eV and the XANES spectra for the Se(-II) sulfide, Se(-I) ferroselite, and elemental Se(0) standards are all visually similar. Based on our comparisons we concluded from the μ-XANES data that the possible Se oxidation states at both POI were Se(-II), Se(-I), or Se(0). Further differentiation in Se speciation was achieved by fitting the μ-EXAFS data.

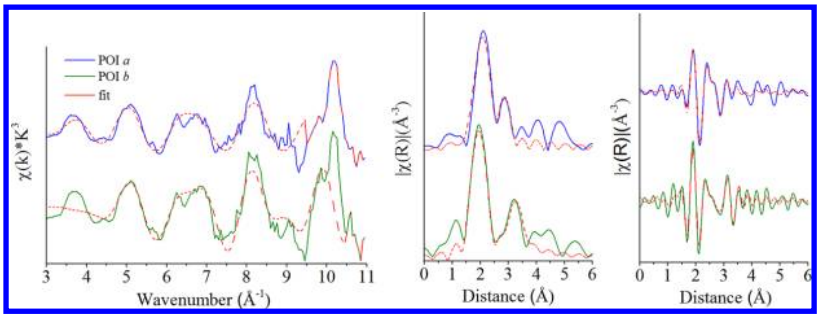

Figure 3. Averaged k^3-weighted (left plot) experimental data and fits (dashed lines) for POI*a* (top) and POI*b* (bottom), real part of the Fourier transform of the spectra (middle) and fits using a k-weight of 3 (right).

Se Chemical Environment and Bonding Characteristics. The μ-EXAFS spectra in k-space (Figure 3) indicated a similar local coordination environment of Se for both POI (see also Figure S9 in the SI with overlaid POI spectra). The spectra are similar over the entire k-space range, with features at ~4.2, 5.7, and 6.5 $Å^{-1}$ apparent in both spectra. However, the Fourier transforms indicate that Se was not present in exactly the same bonding environment in POI*a* and POI*b*. Sample spectra exhibited noisier and more complex oscillations compared to the standards (Figure 3 and in Figure S7 in the SI) due to the lower concentration of Se (max 670 ppm in euhedral grains; Table 2). The fingerprints in k-space between both POI and the synthetic ferroselite[29] showed that both spectra were comparable in phase but with smaller oscillatory amplitudes at low wavenumbers. The sample spectra were clearly out of phase with the seleno-L-cysteine, Se sulfide, and elemental Se standards (Figures S7 and S10 in the SI).

Our fit of the POI*a* spectrum consisted of four single scattering paths (Table 3 and Figure 3) with bond distances consistent with those of S−S and S−Fe in pyrite (where $S-S_1$ = 2.18 Å, $S-Fe_1$ = 2.26 Å, $S-S_2$ = 3.07 Å, and $S-S_2$ = 3.32 Å)[30] but invoking a substitution of S by Se[30] that resulted in a local expansion of 8% in the first shell ($Se-S_1$) and 4% in all the others. The sum of the modeled bond distances (11.351 Å) is very close to that of the pyrite structure (10.830 Å); however, it is expanded as a result of S substitution with Se, where Se has a larger atomic radii compared to S. POI*b* data were fitted (Table 3) using five single scattering paths, four corresponding to the theoretical structure of ferroselite[31] ($Se-Fe_1$ = 2.35 Å, $Se-Fe_2$ = 2.38 Å, $Se-Se_2$ = 3.40 Å, and $Se-Se_3$ = 3.58 Å) and one single scattering path (Se−S=3.07 Å) corresponding to the pyrite structure.[30] The first two Se−Fe paths contributed entirely to the first peak of the Fourier transform (involving 3 Fe atoms, Table 3), and the remaining two Se−Se paths plus the Se−S path contributed to the second peak (individual path contributions in Figure S11 in the SI). The Se−Fe bond distances (average 2.31 Å) are shorter than in the theoretical structure of ferroselite[31] (average 2.37 Å, Se−Fe = 2.35 Å with one Fe and Se−Fe = 2.38 Å with 2 Fe) and are also shorter than in the fit to synthetic ferroselite reported by Ryser et al.[29] (Se−Fe average 2.38 Å). We attribute our somewhat short Se−Fe bond distance to the fact that we are fitting a complex natural sample that likely slightly differs in crystal structure to a theoretical model or indeed a synthetic precipitate. In fact, Ryser et al.,[29] when fitting Se in their sample, fit to a ferroselite polymorph (dzharkenite) with a first shell attributed to Se−Se at an average bond distance of 2.28 Å, but our fit showed no Se−Se bonds in the first shell.

Table 3. Local Coordination Environment of Se at POI*a* and POI*b* As Determined by Se K-Edge μ-EXAFS Analysis

	path	N^a	R (Å)^b	σ^2 (Å^2)	R-factor	χ^2
$POIa_{euhedral}$	Se−S	1	2.344 ± 0.003	0.003	0.024	205
	Se−Fe	3	2.354 ± 0.003	0.004		
	Se−S	6	3.198 ± 0.003	0.018		
	Se−Se	4	3.455 ± 0.003	0.018		
$POIb_{framboidal}$	Se−Fe	1	2.284 ± 0.004	0.005	0.022	92
	Se−Fe	2	2.318 ± 0.004	0.005		
	Se−S	2	2.987 ± 0.004	0.009		
	Se−Se	4	3.308 ± 0.004	0.002		
	Se−Se	6	3.479 ± 0.004	0.002		

^{a}Degeneracy (coordination number for single paths). ^{b}Interatomic distances.

We performed Se speciation analysis on POI clearly identified as pyrite and expected the local coordination environment to reflect structural Se substitution for S as previously suggested.[22,23] However, our μ-EXAFS analysis (Table 3 and Figure 3) suggested that the Se coordination environment in pyrite was dependent on the pyrite morphology. In euhedral grains (POI*a*) Se was substituted for S in the pyrite structure as previously suggested, but in framboidal grains (POI*b*) the local environment of Se was akin to Se in a discrete ferroselite-like species ($FeSe_x$).

DISCUSSION

Se in Shales and in the Pyrite Fraction. The UK samples are typical shale rocks with relatively low bulk Se concentrations (<1 to ~10 μg/g). Sequential extractions, microprobe analyses, and μ-XRF data clearly demonstrated that the main Se host in these samples was pyrite, with sequential extraction also suggesting minor Se associated with organic matter. As such our results strengthen previous data[32−34] that reported Se in carbonaceous shales highly associated with pyrite and organic matter. In the highest bulk Se samples (UK-1 and UK-2), 50 and 74% of the Se (Table 1) was associated with pyrite, and μ-XRF maps only showed high Se values on pyrite and low Se values in the organic matter or silicates matrix, corroborating the minor Se-organic matter association. The strong μ-scale correlations between Se, As, Ni, and Cu in the pyrite grains also confirm the Se-pyrite link, as these metalloids and metals are most often solely enriched in pyrite and not in organic matter.[32,35] Of crucial importance, our results also show that variations in total Se concentrations in typical shales do not solely depend on total S and organic C contents, but in addition there is a clear link between Se concentration and pyrite grain morphology (Table 2 and Table S6). Microprobe analyses showed that euhedral

pyrites contained overall far higher concentrations of Se compared to framboidal pyrites (Table 2 and Table S8 in SI) and that in fact no (<90 ppm detection limit) Se was associated with any organic matter or silicate grains. There is an apparent mismatch between the proportion of Se associated with nonpyrite fractions in the sequential exactions (Table 1) and the absence of Se in the nonpyrite matrix measured with the microprobe. This is because sequential extractions measure bulk Se which is diffusely distributed in the nonpyrite matrix, while microprobe point analyses will only show high values in localized grains (i.e., pyrite), where Se is highly concentrated. In Matamoros et al.[16] we demonstrated that even if organic C contents (2−5%) were higher than pyrite contents (1−3%), Se was still preferentially associated with pyrite. Thus, the data in our current study, combined with literature knowledge about pyrite formation pathways,[35−40] helps us understand how Se is sequestered into, and released from, pyrite in shales.

Pyrite Formation in Shales and Links to Se Speciation. The grain-level concentrations and speciation of Se depended on whether pyrite was present in framboidal or euhedral morphology (Table 2, Table 3, and Table S8). This difference can be attributed to variations in chemical environments and formation pathways of the two morphologies or the effects of diagenesis.[41]

In natural settings framboidal pyrite is known to form rapidly at the chemocline where Fe and S sources are readily available.[36−38] Here Se will be present as an oxic species, in either aqueous or sorbed form.[18−20] Framboids are difficult to synthesize in the laboratory,[39] and no experimental evidence on Se-framboidal interactions is available. Some experimental studies used iron sulfides (e.g., mackinawite,[42] pyrite[18−20,43]) and sorbed Se onto them. When synthetic pyrite was used, the Se was coreduced leading to the formation of ferroselite FeSe(-I)$_x$.[18,42,44] Our current Se-edge μ-XAS data on natural framboids shows an independent ferroselite-like FeSe(-I)$_x$ species as the dominant Se form associated with our framboids (Figure 3). Combining the experimental evidence with our μ-XAS data suggests that coreduction during framboid formation must be the dominant pathway to producing ferroselite in natural framboidal pyrites formation environments.

Euhedral pyrite grains form more slowly via the supply of low levels of external, less reactive Fe and Se.[35,45−48] The source for these Fe/Se species is diffusive transport, followed by their reduction and subsequent sequestration into the euhedral crystal structure.[23,49] Our μ−XAS data (Figure 3) clearly shows a Se for S replacement in our euhedral pyrite, supporting the slow growth by coupled diffusion/reduction, which also leads to higher average Se concentrations in euhedral grains (Table 2).

If such euhedral grains formed through framboidal aggregate recrystallization,[36,46,47] we would expect Se to retain the ferroselite, FeSe(-I)$_x$ speciation as in the framboids. However, this is not the case as our euhedral POI*a* μ-XAS evidence Se replacing S in the pyrite structure (Figure 3 and Table 3).

We demonstrated that Se speciation in pyrite in shales is dependent on pyrite morphology, but further spatially resolved speciation studies in other shale samples are necessary to evaluate if such a morphology-dependent speciation is universal or only linked to pyrites formed through similar sedimentary processes.[47,48]

The Formation and Importance of FeSe$_x$ Species in Framboidal Pyrite. In modern marine sediments the most frequent pyrite morphology is framboidal,[50] and we demonstrate Se in this morphology to exist as ferroselite, which is thermodynamically stable over a wide range of pH and low oxygen conditions (Figure S12 left in the SI).[51,52]

The formation of ferroselite has been studied experimentally under both abiotic and biotic conditions. Naveau et al.[18] investigated the adsorption of aqueous Se(IV) and Se(-II) onto natural and synthetic pyrites and showed that Se is first reduced in solution and then it adsorbs onto the pyrite surface. This reduction must be counterbalanced by the oxidation of reduced iron species in pyrite. Charlet et al.[43] demonstrated that ferroselite ($FeSe_2$) and Se(0) can form when reacting synthetic nanophase pyrite with Se(IV) and Se(VI) solutions. However, in another study from the same group[19] the reduction of aqueous Se(IV) by pyrite was corroborated, but the formation of ferroselite was excluded, instead elemental selenium was suggested as the Se species at slightly acidic and neutral pH (4.5−6.6). The ability of other ferrous minerals (e.g., green rust, mackinawite, siderite, or troilite) to reduce aqueous Se(IV) and Se(VI) to elemental Se and selenides has been inferred to be coupled to the oxidation of S(-II)/Fe(II) to S(0)/Fe(III) in such phases.[20,42−44,53,54] Other evidence suggests microbial metabolic processes may be responsible for the formation of selenides[53,54] and ferroselite in particular. Herbel et al.[53] using XAS analyses of selenite-respiring bacteria showed initially a microbial reduction of selenite to elemental Se and a further reduction to Se(-II) species and the formation of FeSe$_x$ precipitates.

Combining these observations with our results, we suggest that in our shale sample the FeSe$_x$ species formed coevally with the framboids at the chemocline where microbial processes dominate and through reduction of local aqueous Se. During subsequent diagenesis or weathering FeSe$_x$ will be highly soluble at low pH and intermediate redox conditions (Figure S12 in the SI), thus allowing for easy Se release and subsequent transport or readsorption onto other minerals.

Implications for Se release. Our Se mobility data from the sequential extractions showed Se easily liberated from oxides, clay minerals, and carbonates. When reacting our samples with mildly acidic reagents (Protocol A: water, exchangeable, Se(0) and acetic extractions − Figure S3 in the SI) 10% of the total Se was easily released. In a weathering environment characterized by slightly acid to neutral pH's, this will certainly release Se from shales into local groundwaters. The largest proportion of Se, however, was associated with pyrite, which is the largest and most reactive Se host phase in shales. Oxidative pyrite weathering from shales together with dissolution of the more soluble FeSe$_x$ will therefore control the delivery of Se to aquifers and/or soils. Specifically, such dissolution processes result in the redistribution of iron into Fe oxyhydroxides (e.g., ferrihydrite) or Fe oxyhydroxide sulfates (e.g., schwertmannite) and the production of sulfuric acid leading to acidic[55] soils. The associated Se species (FeSe$_x$ and Se in the euhedral pyrite structure) will co-oxidize to form elemental Se, and with further oxidation these will convert to more toxic and bioavailable selenite or selenate species[6,8] (Figure S12 right in the SI). Selenite species behave analogously to As species[56−58] when interacting with minerals, and thus once in the aqueous medium, selenite may readsorb onto FeOOH particles at acidic pH conditions or remain bioavailable as free aqueous species in aquifers and thus be transferred to the human food chain with harmful effects.

The rates at which the different pyrite morphologies are oxidized during shale weathering will govern the release rates of Se, because framboidal pyrites (made of microcrysts with a large surface area) are weathered faster than euhedral often larger pyrites crystals. Thus, in shales with high framboidal pyrite

contents[50] that are oxidatively weathered, Se release will be maximal where secondary iron minerals that can sequester the released Se are limited and/or where ambient pH is neutral to alkaline.

Se as Potential Proxy for Past Environmental Conditions. Framboid size distribution is an often used proxy for redox conditions in marine sediments.[50] Recently, the use of Se isotopes was suggested as another powerful palaeoenvironmental proxy.[5,12,59] Specifically, Mitchell et al.[12] suggested a link between bulk Se/TOC ratios (mol/mol) and Se isotopic values as a first step toward such a proxy. They also noted that the lack of Se speciation information is hindering the full use of Se isotopes as a palaeoproxy. We did not analyze the Se isotope compositions in our shales, but our bulk Se/TOC ratios (Table S6 in the SI) varied between 2.48×10^{-6} and 8.74×10^{-5}, which lie within the typical range suggested for shales[12] Our data shows a clear link between Se and pyrite and a clear difference in Se speciation in framboidal and euhedral grains. Such a host-fraction differentiation and a morphology-resolved speciation analyses, albeit difficult and time-consuming, could much improve the use of Se as a palaeoenvironmental proxy. Therefore, we infer that to demonstrate the power of Se as a potential proxy in both modern and ancient settings, measuring only bulk Se isotopic values of rocks are insufficient. In a first step toward a better Se palaeoproxy, we propose that bulk Se isotopic analyses need to be combined with spatially and morphologically resolved Se speciation analyses as described in the current study. A further step—that may currently not yet be feasible technologically—would be a spatially and host-fraction differentiated and also pyrite morphology-resolved Se isotopic fingerprinting, combined with coresolved Se speciation analyses. Such a combined approach would indeed pave the way to a very powerful Se palaeo-oceanographic proxy.

■ ASSOCIATED CONTENT

Ⓢ Supporting Information

Sample details; bulk characterization; Se distribution from sequential extractions and trace elements; euhedral and framboidal pyrite microprobe analyses; correlation plots of μ-XRF areas; details of μ-XANES and μ-EXAFS analyses; thermodynamic modeling. This material is available free of charge via the Internet at http://pubs.acs.org.

■ AUTHOR INFORMATION

Corresponding Authors

*Phone: +44 113 3435220. Fax: +44 113 3435259. E-mail: A. MatamorosVeloza@leeds.ac.uk.

*Phone: +44 113 3435220. Fax: +44 113 3435259. E-mail: L.G. Benning@leeds.ac.uk.

Notes

The authors declare no competing financial interest.

■ ACKNOWLEDGMENTS

We acknowledge funding from a Dorothy Hodgkin/EPSRC Scholarship for AMV and from the UK Science and Technology Council (STFC) for beamtime (Grant EC 870 to L.G.B.). The authors wish to thank Fred Mosselmans, Tina Geraki, and Loredana Brinza from Diamond Light Source Ltd. for their tireless assistance and support during XAS data collection and processing.

■ REFERENCES

(1) Schrauzer, G. N. Selenomethionine. A review of its nutritional significance, metabolism and toxicity. *J. Nutr.* **2000**, *130*, 1653−1656.

(2) British Nutrition Foundation. http://britishnutrition.org.uk/home.asp?siteld=43&sectionld=s (accessed June 10, 2014).

(3) Vinceti, M.; Nacci, G.; Rocchi, E.; Cassinadri, T.; Vivoli, R.; Marchesi, C.; Bergomi, M. Mortality in a population with long term exposure to inorganic selenium via drinking water. *J. Clin. Epidemiol.* **2000**, *53*, 1062−1068.

(4) Nuttall, K. L. Review: Evaluating Selenium Poisoning. *Ann. Clin. Lab. Sci.* **2006**, *36* (4), 409−420.

(5) Zhu, J.; Johnson, T. M.; Clark, S. K.; Zhu, X.; Wang, X. Selenium redox cycling during weathering of Se-rich shales: A selenium isotope study. *Geochim. Cosmochim. Acta* **2014**, *126*, 228−249.

(6) Winkel, L. H. E.; Johnson, C. A.; Lenz, M.; Grundi, T.; Leupin, O. X.; Amini, M.; Charlet, L. Environmental Selenium Research - from Microscopic Processes to Global Understanding. *Environ. Sci. Technol.* **2011**, *46* (2), 571−579.

(7) U.S. Department of Human Health and Services. *Toxicological profile for selenium*; P.H. Service and A.f.T.S.a.D. Registry, Eds.; Department Health and Human Services, Public Health Service, Agency for Toxic Substances and Disease Registry: 2003.

(8) Plant, J. A.; Kinniburgh, P. L.; Smedley, P. L.; Fordyce, F. M.; Klinck, B. A. Arsenic and Selenium. In *Treatise on geochemistry*; Holland, H. D., Turekian, K. K., Eds.; Elsevier-Pergamon: Amsterdam; London, 2003; Vol. *9*.

(9) Bar Yosef, B. Selenium desorption from Ca-kaolinite. *Commun. Soil Sci. Plant Anal.* **1987**, *18* (7), 771−771.

(10) Zawislanski, P. T.; Benson, S. M.; Terberg, R.; Borglin, S. E. Selenium speciation, solubility, and mobility in land-disposed dredged sediments. *Environ. Sci. Technol.* **2003**, *37*, 2415−2420.

(11) Allaway, W. H.; Cary, E. E.; Ehlig, C. F. The cycling of low levels of selenium in soils, plants and animals. Chapter 17 In *Selenium in Biomedicine*; Muth, O. H., Oldfield, J. E., Weswig, P. H., Eds.; AVI Publishing: Westport, CT, 1967.

(12) Mitchell, K.; Mason, P. D. R.; Van Capellen, P.; Johnson, T. M.; Gill, B. C.; Owens, J. D.; Diaz, J.; Ingall, E. D.; Reichart, G. J.; Lyons, T. W. Selenium as paleo-oceanographic proxy: A first assessment. *Geochim. Cosmochim. Acta* **2012**, *89*, 302−317.

(13) Fordyce, F. M.; Guangdi, Z.; Green, K.; Xinping, L. Soil, grain and water chemistry in relation to human selenium-responsive diseases in Enshi District, China. *Appl. Geochem.* **2000**, *15* (1), 117−132.

(14) Qin, H.; Zhu, J.; Su, H. Selenium fractions in organic matter from Se-rich soils and weathered stone coal in selenosis areas of China. *Chemosphere* **2012**, *86* (6), 626−633.

(15) Wen, H.; Carignan, J.; Qiu, Y.; Liu, S. Selenium speciation in kerogen from two chinese selenium deposits: environmental implications. *Environ. Sci. Technol.* **2006**, *40* (4), 1126−1132.

(16) Matamoros-Veloza, A.; Newton, R. J.; Benning, L. G. What controls selenium release during shale weathering? *Appl. Geochem.* **2011**, *26*, S222−S226.

(17) Kulp, T. R.; Pratt, L. M. Speciation and weathering of selenium in upper cretaceous Chalk and shale from South Dakota and Wyoming, USA. *Geochim. Cosmochim. Acta* **2004**, *68* (18), 3687−3701.

(18) Naveau, A.; Monteil-Rivera, F.; Guillon, E.; Dumonceau, J. Interactions of Aqueous Selenium (-II) and (IV) with Metallic Sulfide Surfaces. *Environ. Sci. Technol.* **2007**, *41* (15), 5376−5382.

(19) Kang, M.; Chen, F.; Wu, S.; Yang, Y.; Bruggeman, C.; Charlet, L. Effect of pH on Aqueous Se(IV) Reduction by Pyrite. *Environ. Sci. Technol.* **2011**, *45* (7), 2704−2710.

(20) Breynaert, E.; Bruggeman, C.; Maes, A. XANES-EXAFS Analysis of Se solid-phase reaction products formed upon contacting Se(IV) with FeS_2 and FeS. *Environ. Sci. Technol.* **2008**, *42*, 3595−3601.

(21) Mitchell, K.; Couture, R. M.; Johnson, T. M.; Mason, P. R. D.; Van Cappellen, P. Selenium sorption and isotope fractionation: Iron(III) oxides versus iron(II) sulfides. *Chem. Geol.* **2013**, *342*, 21−28.

(22) Strawn, D.; Doner, H.; Zavarin, M.; McHugo, S. Microscale investigation into the geochemistry of arsenic, selenium, and iron in soil developed in pyritic shale materials. *Geoderma* **2002**, *108*, 237−257.

(23) Presser, T. S.; Swain, W. C. Geochemical evidence for selenium mobilization by the weathering of pyritic shale, San Joaquin Valley, California, USA. *Appl. Geochem.* **1990**, *5*, 703−717.
(24) Brumhead, D. *Geology Explained in the Yorkshire Dales and on the Yorkshire Coast*; David and Charles: London, 1979.
(25) Fisher, Q. J.; Wignall, P. B. Palaeoenvironmental controls on the uranium distribution in an Upper Carboniferous black shale (Gastrioceras listeri Marine Band) and associated strata. *Chem. Geol.* **2001**, *175*, 605−621.
(26) Lussier, C.; Veiga, V.; Baldwin, S. The geochemistry of selenium associated with coal waste in the Elk River Valley, Canada. *Environ. Geol.* **2003**, *44*, 905−913.
(27) Newton, R. J.; Bottrell, S. H.; Dean, S. P.; Hatfield, D.; Raiswell, R. An evaluation of the use of the chromous chloride reduction method for isotopic analyses of pyrite in rocks and sediment. *Chem. Geol.* **1995**, *125*, 317−320.
(28) Calvo, C.; Gillespie, R. J.; Vekris, J. E.; Ng, H. N. Title Structure of monoclinic sulphur-selenium Se_3S_5. *Acta Crystallogr., Sect. B: Struct. Crystallogr. Cryst. Chem.* **1978**, *B34*, 911−912.
(29) Ryser, A. L.; Strawn, D. G.; Marcus, M. S.; Johnson-Maynard, J. L.; Gunter, M. E.; Möller, G. Micro-spectroscopic investigation of selenium-bearing minerals from the Western US Phosphate Resource Area. *Geochem. Trans.* **2005**, *6* (1), 1−11.
(30) Brostigen, G.; Kjekshus, A. Redetermined crystal structure of FeS2 (pyrite). *Acta Chem. Scand.* **1969**, *23*, 2186−2188.
(31) Bur'yanova, Z.; Komkov, A. I. Ferroselite-a new mineral. *Dokl. Akad. Nauk SSSR* **1955**, *105*, 812−813 (Russian); *Chem. Abstr.* **1955**, *50*, 9239..
(32) Tuttle, M. L. W.; Breit, G. N.; Goldhaber, M. B. Weathering of the New Albany Shale, Kentucky: II. Redistribution of minor and trace elements. *Appl. Geochem.* **2009**, *24*, 1565−1578.
(33) Morse, J. W.; Luther, G. W. Chemical influences on trace metal sulfide interactions in anoxic sediments. *Geochim. Cosmochim. Acta* **1999**, *63* (19−20), 3373−3378.
(34) Diehl, S. F.; Goldhaber, M. B.; Koenig, A. E.; Tuttle, M. L. W.; Ruppert, L. F. *Concentration of arsenic, selenium, and other trace elements in pyrite in appalachian coals of Alabama and Kentucky*. National Meeting of the American Society of Mining and Reclamation, June 19−23, 2005. Published by ASMR, 3134 Montavesta Rd., Lexington, KY 40502, 2005.
(35) Berner, Z. A.; Puchelt, H.; Nöltner, T.; Kramar, U. T. Z. Pyrite geo-chemistry in the Toarcian Posidonia Shale of south-west Germany: Evidence for contrasting trace-element patterns of diagenetic and syngenetic pyrites. *Sedimentology* **2013**, *60*, 548−573.
(36) Goldhaber, M. B. *Sulfur-rich sediments in Treatise on Geochemistry (7) Sediments, diagenesis and Sedimentary rocks*; Elsevier Pergamon: 2003.
(37) Wilkin, R. T.; Barnes, H. L.; Brantley, S. L. The size distribution of framboidal pyrite in modern sediments: An indicator of redox conditions. *Geochim. Cosmochim. Acta* **1996**, *60* (20), 3897−3912.
(38) Wilkin, R. T.; Arthur, M. A.; Dean, W. E. History of water-column anoxia in the Black Sea indicated by pyrite framboid size distributions. *Earth Planet Sci. Lett.* **1997**, *148* (5), 17−525.
(39) Wilkin, R. T.; Barnes, H. L. Pyrite formation by reactions of iron monosulfides with dissolved inorganic and organic sulfur species. *Geochim. Cosmochim. Acta* **1996**, *60* (21), 4167−4179.
(40) Benning, L. G.; Wilkin, R. T.; Barnes, H. L. Reaction pathways in the FeS system below 100°C. *Chem. Geol.* **2000**, *167* (1−2), 25−51.
(41) Love, L. G. Micro-organic material with diagenetic pyrite from the Lower Proterozoic Mount Isa Shale and a Carboniferous shale. *Proc. Yorks. Geol. Soc.* **1965**, *35*, 187−202.
(42) Scheinost, A. C.; Charlet, L. Selenite reduction by mackinawite, magnetite and siderite: XAS characterization of nanosized redox products. *Environ. Sci. Technol.* **2008**, *4*, 1984−1989.
(43) Charlet, L.; Kang, M.; Bardelli, F.; Kirsch, R.; Géhin, A.; Grenèche, J. M.; Chen, F. Nanocomposite Pyrite−Greigite Reactivity toward Se(IV)/Se(VI). *Environ. Sci. Technol.* **2012**, *46* (9), 4869−4876.
(44) Howard, J. H. Geochemistry of selenium: formation of ferroselite and selenium behavior in the vicinity of oxidizing sulfide and uranium deposits. *Geochim. Cosmochim. Acta* **1977**, *41*, 1665 −1678.
(45) Raiswell, R.; Plant, J. The incorporation of trace elements into pyrite during diagenesis of black shales, Yorkshire, England. *Econ. Geol.* **1980**, *15*, 684−699.
(46) Wang, Q.; Morse, J. W. Pyrite formation under conditions approximating those in anoxic sediments. I. Pathway and morphology. *Mar. Chem.* **1996**, *52*, 99−121.
(47) Morse, J. W.; Wang, Q. Pyrite formation under conditions approximating those in anoxic sediments. *Mar. Chem.* **1997**, *57* (3−4), 187−193.
(48) Murowchick, J. B.; Barnes, H. L. Effects of temperature and degree of supersaturation on pyrite morphology. *Am. Mineral.* **1987**, *72*, 1241−1250.
(49) Diener, A.; Neumann, T.; Kramar, U.; Schild, D. Structure of selenium incorporated in pyrite and mackinawite as determined by XAFS analyses. *J. Contam. Hydrol.* **2012**, *133*, 30−39.
(50) Wignall, P. B.; Newton, R. Pyrite framboid diameter as a measure of oxygen deficiency in ancient mudrocks. *Am. J. Sci.* **1998**, *298*, 537−552.
(51) Scheinost, A. C.; Kirsch, R.; Banerjee, D.; Fernandez-Martinez, A.; Zaenker, H.; Funke, H.; Charlet, L. X-ray absorption and photoelectron spectroscopy investigation of selenite reduction by Fe-II-bearing minerals. *J. Contam. Hydrol.* **2008**, *102* (3−4), 228−245.
(52) Bruggeman, C.; Maes, A.; Vancluysen, J.; Vandemussele, P. Selenite reduction in Boom clay: effect of FeS2, clay minerals and dissolved organic matter. *Environ. Pollut.* **2005**, *137*, 209−221.
(53) Herbel, M. J.; Blum, J. S.; Oremland, R. S.; Borglin, S. E. Reduction of elemental selenium to selenide: Experiments with anoxic sediments and bacteria that respire Se-oxyanions. *Geomicrobiol. J.* **2003**, *20*, 587−602.
(54) Bacon, M.; Ingledew, W. J. The reductive reactions of Thiobacillus ferrooxidans on sulphur and selenium. *FEMS Microbiol. Lett.* **1989**, *58*, 189−194.
(55) Lavergren, U. Black shale as a metal contamination source. *ESS Bull.* **2005**, *3* (1), 18−31.
(56) Dudas, M. J. Enriched levels of arsenic in post-active sulphate soils in Alberta. *Soil Sci. Soc. Am. J.* **1984**, *48* (6), 1451−1452.
(57) Nickson, R.; McArthur, J.; Burgess, W.; Ahmed, K. M.; Ravenscroft, P.; Rahman, M. Mechanism of arsenic release to groundwater, Bangladesh and West Bengal. *Appl. Geochem.* **2000**, *15*, 403−413.
(58) British Geological Survey Report WC/00/19. *Arsenic contamination of groundwater in Bangladesh*; Kinninburgh, D. G., Smedley, P. L., Eds; 2001.
(59) Sageman, B. B.; Lyons, T. W. Geochemistry of fine-grained sediments and sedimentary rocks. In *Treatise on geochemistry*; Holland, H. D., Turekian, K. K., Eds.; Elsevier-Pergamon: Amsterdam; London, 2003; Vol. 7.